The structure of dark and luminous matter in early-type galaxies

Weijmans, A.M.

Citation

Weijmans, A. M. (2009, September 9). *The structure of dark and luminous matter in early-type galaxies*. Retrieved from https://hdl.handle.net/1887/13970

Chapter 3

Stellar velocity profiles and line strengths out to four effective radii in the early-type galaxies NGC 3379 and NGC 821

We use the integral-field spectrograph SAURON to measure the stellar line-of-sight velocity distribution and absorption line strengths out to four effective radii (R_e) in the early-type galaxies NGC 3379 and NGC 821. With our newly developed observing technique we can now probe these faint regions in galaxies that were previously not accessible with traditional long-slit spectroscopy. We make optimal use of the large field-of-view and high throughput of the spectrograph: by adding the signal of all $\sim$1400 lenslets into one spectrum, we obtain sufficient signal-to-noise in a few hours of observing time to reliably measure the absorption line kinematics and line strengths out to large radius.

We find that the line strength gradients observed within 1 R_e remain constant out to at least 4 R_e, which puts constraints on the merger histories of these galaxies. The stellar halo populations are old and metal-poor. By constructing orbit-based Schwarzschild dynamical models we find that dark matter is needed to explain the observed kinematics in NGC 3379 and NGC 821, with 30 - 50% of the total matter being dark within 4 R_e. The radial anisotropy in our best-fit halo models is less than in our models without halo, due to differences in orbital structure. The halo also has an effect on the Mg b -V_{esc} relation: its slope is steeper when a dark halo is added to the model.

Anne-Marie Weijmans, Michele Cappellari, Roland Bacon, P. Tim de Zeeuw,
Eric Emsellem, Jesús Falcón-Barroso, Harald Kuntschner, Richard M. McDermid,
Remco C. E. van den Bosch & Glenn van de Ven
Monthly Notices of the Royal Astronomical Society, in press (2009)

3.1 Introduction

According to the current galaxy formation paradigm, galaxies should be embedded in massive dark matter haloes (e.g. Kauffmann & van den Bosch 2002; Springel et al. 2005). For spiral galaxies, these haloes have indeed been observationally confirmed, by determining their influence on the kinematics of the H I discs that surround most of these galaxies (see e.g. van Albada et al. 1985). Early-type galaxies often lack these large gas discs, and therefore their dark matter haloes are more difficult to probe. Although some early-type galaxies do have regular H I structures that have been used to identify a dark matter halo (e.g. Bertola et al. 1993; Franx, van Gorkom & de Zeeuw 1994; Oosterloo et al. 2002; Weijmans et al. 2008) and recent sensitive radio observations have shown that H I in these galaxies is more common than previously thought (e.g. Morganti et al. 2006), for the majority of early-type galaxies we need to employ other tracers to determine the dark matter content.

Stellar kinematics are a reliable tracer of the gravitational potential in galaxies. Unfortunately, traditional long-slit spectroscopy seldom reaches beyond two half-light or effective radii (R_e), because the necessary signal-to-noise ratio (S/N) is difficult to achieve in this regime. In the central parts of galaxies this is not an issue, and it has been shown by various studies that in early-type galaxies within one R_e the luminous matter still dominates over the dark matter: only 10 - 50 per cent of the total mass is dark (Gerhard et al. 2001; Cappellari et al. 2006; Thomas et al. 2007). These data however do not cover the outer regions of galaxies, where the dark matter is supposed to dominate. Models of early-type galaxies based on long-slit stellar kinematics extending to larger radii are not always conclusive, but indicate that a dark halo is required in some individual cases (e.g. Carollo et al. 1995; Rix et al. 1997).

To probe the gravitational potential at larger radii (outside one R_e), we can resort to gravitational lensing (e.g. Koopmans et al. 2006; Gavazzi et al. 2007), X-ray emission (e.g. O'Sullivan & Ponman 2004; Humphrey et al. 2006) or discrete tracers such as globular clusters (e.g. Côté et al. 2003; Bridges et al. 2006) or planetary nebulae (e.g. Romanowsky et al. 2003; Douglas et al. 2007; Napolitano et al. 2009). Interestingly, Romanowsky et al. (2003) found that models of their sample of three intermediate luminosity early-type galaxies only required a small amount of dark matter, if any at all. Dekel et al. (2005) subsequently argued that the observed kinematics of the planetary nebulae (PNe) could also be explained by invoking radial anisotropy, and therefore do not exclude a dark halo (see also Binney & Mamon 1982). Douglas et al. (2007) presented newly reduced PNe kinematics for one of the galaxies of the Romanowksy et al. sample

Parameter	NGC 821	NGC 3379
Morphological Type	E6?	E1
M_B (mag)	-20.74	-20.57
Effective $B-V$ (mag)	0.87	0.93
Photometric PA (°)	32	68
Distance modulus (mag)	31.85	30.06
Distance (Mpc)	23.4	10.3
Distance scale (pc arcsec^{-1})	114	50
Effective radius (arcsec)	39	42
Systemic velocity (km/s)	1726	930

Table 3.1 — Properties of NGC 821 and NGC 3379. Magnitude and colour are taken from the Lyon/Meudon Extra galactic Database (LEDA). The distance modulus was derived from surface brightness fluctuation measurements by Tonry et al. (2001). Note that 0.06 mag is subtracted to adjust to the Cepheid zeropoint of Freedman et al. (2001); see Mei et al. (2005), section 3.3, for a discussion. The effective radius and position angle are taken from Cappellari et al. (2007).

(NGC 3379) and found the dark matter fraction within 5 R_e to be less than 40 per cent, which is significantly lower than what is predicted by ΛCDM models. Napolitano et al. (2009) reached similar conclusions modeling PNe kinematics in the elliptical galaxy NGC 4494 and suggested that intermediate-luminosity galaxies are surrounded by low concentration haloes, while some high-mass ellipticals could have more strongly concentrated haloes. De Lorenzi et al. (2009) presented mass models of NGC 3379 based on the PNe kinematics of Douglas et al. (2007), combined with long-slit and central SAURON integral-field data, and concluded that they can fit the data with a range of mass distributions, depending on the anisotropy. They did not exclude a dark matter halo with a strong radially anisotropic outer envelope, that is still consistent with merger models within the ΛCDM paradigm.

We observed two of the galaxies of the Romanowsky et al. (2003) sample, NGC 3379 and NGC 821, with the SAURON integral-field unit (IFU), to measure the line-of-sight velocity distribution (LOSVD) at large radii (3-4 R_e). We took advantage of the high throughput and large field-of-view of SAURON (41×33 arcsec^2) and used the IFU as a "photon collector": for each observation we co-added all spectra within one field to acquire enough S/N to measure the LOSVD up to the fourth Gauss-Hermite moment h_4. These higher order moments are key to breaking the mass-anisotropy degeneracy when constructing mass models and determining the dark matter content of galaxies (e.g. Gerhard 1993). Apart from

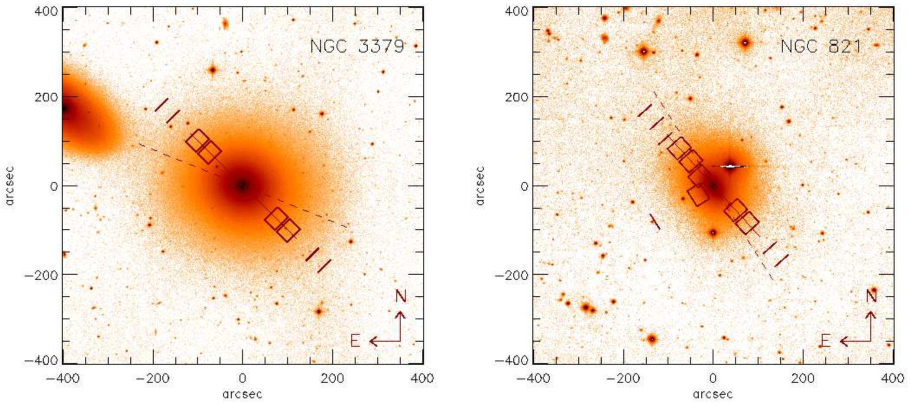

Figure 3.1 — Positions of our observed fields in NGC 3379 (left) and NGC 821 (right). The red boxes denote each SAURON field of view. The skylenslets (red short thick lines) are aligned with the long side of the SAURON field, at a distance of two arcminutes. SAURON was orientated such that the skylenslets pointed away from the galaxy nucleus. The fields are not exactly aligned with the major axis of the galaxy (denoted by the dashed line) to minimize the contamination of foreground stars and neighbouring galaxies. The underlying images were obtained with the 1.3-m McGraw-Hill Telescope at MDM Observatory.

the LOSVD, we also obtained line strengths from our spectra, allowing us to study line strength gradients out to large radii and constraining the properties of the stellar halo populations. Both NGC 3379 and NGC 821 are well studied galaxies, and some of their properties are summarized in Table 3.1. Their central regions have been observed as part of the SAURON survey (de Zeeuw et al. 2002). They are classified as fast rotators (Emsellem et al. 2007) and display regular stellar kinematics.

In section 3.2, we describe our observations and data reduction. We present our spectra and discuss the resulting LOSVD in section 3.3. Section 3.4 is devoted to measuring line strengths and we investigate gradients and the properties of the stellar populations at large radii. In section 3.5 we present our mass models of NGC 3379 and NGC 821 (including a dark matter halo) and connect the dynamical properties with stellar populations by constructing the Mg b - $V_{\rm esc}$ relation. Section 3.6 summarizes and discusses our results.

3.2 Observations and data reduction

We observed four fields in NGC 3379 with SAURON at the William Herschel Telescope at La Palma, Spain, in March 2005. The fields were centred at 2.6 and 3.5 R_e, on opposite sides of the nucleus to allow for an evaluation of the systemic velocity of the system. They were not placed on the major axis of the galaxy but instead on an axis that deviates by 23°. This was done to avoid contamination in our outer field by the neighbouring galaxy NGC 3384. The positions of the fields were chosen such that most of them did not contain foreground stars, and they were oriented such that the skylenslets of SAURON pointed away from the galaxy nucleus, obtaining skyspectra 2 arcminutes away from the SAURON field.

We used a similar strategy to observe six fields in NGC 821 in September 2006. One field was situated on the minor axis, one field at 1 R_e, two fields at opposite sides of the galaxy nucleus at 2 R_e and the last two fields on opposite sides of the nucleus at 3 R_e. Figure 3.1 shows the observed fields in NGC 3379 and NGC 821, and Table 3.2 summarizes their exposure times and exact positions.

The data were reduced using the dedicated XSAURON software (Bacon et al. 2001). The shutter of SAURON malfunctioned during the observing run of NGC 821, and did not close during read-out of the CCD. This did not affect our science frames, whose exposure times of 1800 seconds are long compared to the typical read-out time of the CCD ($\sim$ 30 seconds). However, our calibration frames have shorter exposure times (15 - 60 seconds) and were badly contaminated by light hitting the CCD during read-out. We could therefore not rely on these calibration frames. Instead, we took the calibration frames obtained during the observing run of NGC 3379 and rotated and translated them so that they coincided with the contaminated frames that they would replace. The spectra of NGC 821 were then extracted and flat-fielded using these frames.

We checked that the extraction of the spectra was done accurately, but we found residuals in the frames after flat-fielding. This was to be expected: although the extraction mask is rather stable between observing runs, the flat-field is not. We therefore constructed a superflat by combining our six empty frames with 30 frames of a Lyman α emitting halo, taken during the same run (see Weijmans et al. 2009b for details). Since these 36 frames contain (mostly) empty sky and are offset with respect to each other, their median, smoothed in the spectral direction, proved to be a suitable superflat (see also Bower et al. 2004). Dividing our already flat-fielded spectra by this superflat removed most of the residuals. Coincidently, we could also construct a superflat for our NGC 3379 dataset: immediately after our observing run SAURON was used in the same setup to observe Lyman α emission around high redshift submillimeter galaxies. These frames also consist

Galaxy	Field	R/R_e	T_{exp} (hr)	μ_V (mag/arcsec^2)	S/N	galaxy contr. (per cent)	Comments
NGC 3379	3N	2.6	2.0	23.0	-	-	cloudy conditions, no signal
	3S	2.6	2.5	23.0	29	15	
	4N	3.5	7.5	23.7	16	5	cloudy conditions
	4S	3.5	2.0	23.7	21	13	
NGC 821	minor	1.0	1.5	23.0	58	28	
	1N	0.9	1.5	21.7	57	24	
	2N	1.9	1.5	23.3	12	7	cloudy conditions
	2S	1.9	0.5	23.3	-	-	cloudy conditions, no signal
	3N	2.9	4.0	24.5	-	-	cloudy conditions, no signal
	3S	2.9	4.0	24.5	9	4	

Table 3.2 — Properties of our observed fields in NGC 3379 and NGC 821. The fields are named according to their distance and orientation with respect to the galaxy centre, see Figure 3.1. The surface brightness μ_V is calculated from the MDM images, and can be compared to the sky surface brightness, which in V-band is about 21.7 mag/arcsec^2 in optimal conditions at our observed fields (Benn & Ellison 1998).

mostly of empty sky, and 19 of them were used to create a superflat for NGC 3379.

After superflat-fielding, both datasets were reduced in the standard manner, except that we did not subtract the sky from the spectra. We will take the contribution of the sky into account when fitting the spectra to extract the stellar kinematics (see Section 3.3).

3.3 Stellar kinematics

To extract the stellar kinematics from our spectra, we used the penalized pixel fitting method (pPXF)[1] of Cappellari & Emsellem (2004). This method fits a stellar template spectrum, convolved with a line-of-sight velocity distribution (LOSVD), to the observed galaxy spectrum in pixel space (i.e. logaritmically binned in wavelength). If apart from the mean velocity V and velocity dispersion σ also the Gauss-Hermite moments h_3 and h_4 are fitted, then the solution is biased towards a Gaussian. The amount of biasing can be controlled, and following the recipe described in Cappellari & Emsellem (2004) we found that a penalization factor of $\lambda = 0.5$ gives the best results for our dataset and signal-to-noise.

3.3.1 Method

To find a suitable stellar template to fit our spectra, we co-added all the spectra of the central SAURON fields of NGC 821 and NGC 3379, presented in Emsellem et al. (2004). We then determined the optimal template for these high signal-to-noise spectra as a linear superposition from the full MILES library, containing 945 stars (Sánchez-Blázquez et al. 2006). For NGC 3379, a template consisting of 19 stars was created, and for NGC 821 a template of 21 stars. Template mismatch is negligible, as can be seen in Figure 3.2. We used these templates to measure the stellar kinematics in our spectra at large radii in NGC 3379 and NGC 821. Additive polynomials were included in our fit to compensate for changes in line strengths, which are to be expected over the radial range that we cover. We found that varying the stellar templates gave similar results for the kinematics within the errors.

Since our spectra are very skydominated (see Table 3.2), we did not subtract the sky from our spectra, but instead included the skyspectra obtained by co-adding the spectra observed with the ∼170 skylenslets of SAURON (pointing ∼ 2 arcminutes away from the field of view) for each exposure as separate templates into pPXF. While the stellar template was broadened with the LOSVD, at the

---

[1] available from www-astro.physics.ox.ac.uk/∼mxc/idl/#ppxf

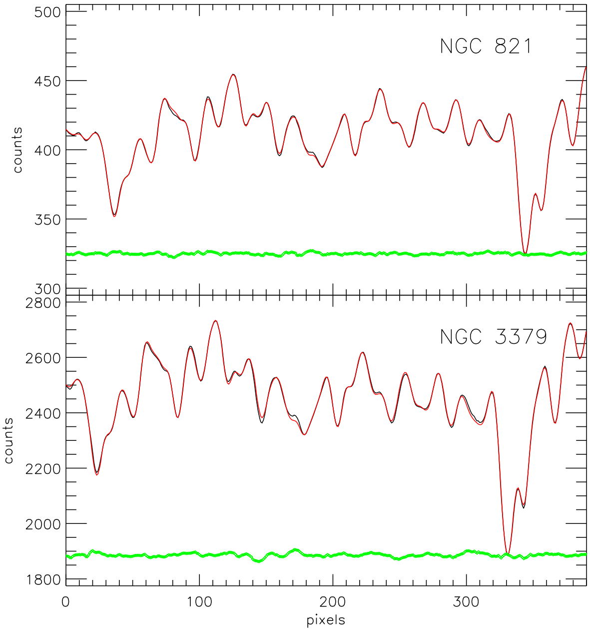

Figure 3.2 — Co-added spectra of NGC 821 and NGC 3379 (black line) and overplotted their optimal stellar templates broadened with the best-fitting LOSVD (grey line). Residuals (grey small dots, shown with offset for presentation purposes) are small, and due to template mismatch.

same time the sky spectra were scaled to minimize the χ^2. The modeled spectrum G_{mod}, with x in pixelspace, is then described by:

$$G_{\mathrm{mod}}(x) = [B \otimes T](x) + \sum_{l=0}^{L} b_l \mathscr{P}_l(x) + \sum_{n=1}^{N} w_n S_n(x), \tag{3.1}$$

with $B(x)$ the broadening function, $T(x)$ the optimal stellar template, $\mathscr{P}_l(x)$ the $L+1$ additive polynomials of degree l with coefficients b_l, and $S_n(x)$ the N sky templates, with weight $w_n \geq 0$ (see also Eq. 3 in Cappellari & Emsellem 2004). By fitting the contribution of the sky in this way instead of subtracting the skyspectra directly, we allow the inclusion of subtle sky variations. We found that especially for the spectra with a low galaxy contribution (see Table 3.2) this improved the fits significantly.

We subtracted the resulting composite skytemplate $\sum_{n=1}^{N} w_n S_n(x)$ from the observed spectrum, and ran pPXF again. Errors are estimated by a Monte Carlo method, where we measured the kinematics from many realisations of the input spectrum, on which we added noise. The noise spectrum was obtained from the difference between our observed spectrum and the best-fit modeled spectrum (G_{mod}). We found that varying the amount of subtracted sky by up to 10 per cent does not affect our measured LOSVD. This shows that our LOSVD parameters are robust to errors in our sky subtraction. We also checked that the measured LOSVD is indeed the LOSVD of the galaxy and not an imprint of the solar spectrum from e.g. zodiacal light: when measuring the LOSVD of the sky templates themselves we measured a velocity offset with respect to the galaxy comparable to the systemic velocity of the system, and a much smaller broadening.

We found that the best fits were obtained by including the skyspectra from the skylenslets, taken simultaneously with our galaxy spectra. Providing the sky spectra of our blank skyfields as templates gave worse results, even though these fields covered a larger sky area than the skylenslets and therefore had higher S/N. This indicates the importance of obtaining simultaneous skyspectra over high S/N, to avoid mismatch due to the variability of the night sky.

Finally, we tested the influence of subtracting residual galaxy light that could be present in our sky spectra, since the skylenslets were pointing at 6 - 7 R_e in the galaxy. The galaxy light at these distances of the nucleus is however very faint, approximately 3-4 mag/arcsec^2 fainter than in the regions where we measure our kinematics. We simulated the effect of subtracting such a weak Gaussian absorption line from our observed line and found that the maximal error we can introduce in this way is 8 km/s in our measured velocity dispersions. This is well within our error bars, and we conclude that this effect is negligible.

3.3.2 NGC 3379

It turned out that one of our fields in NGC 3379, 3N, did not have sufficient signal to measure the LOSVD. The results for the other fields can be found in Figure 3.3 and Table 3.3. The last four columns for Table 3.3 show the results for the LOSVD if we restrict our fit to the first two moments, instead of fitting up to h_4. The results for both fits agree within the errors.

Correcting for barycentric motion, we find that the systemic velocity V_{sys} of the galaxy measured from the central field (presented by Emsellem et al. 2004) is 930 ± 2 km/s. This agrees with V_{sys} as determined from the 3S and 3N field pair: although we could not measure the velocity dispersion from the spectrum in 3N, we were able to determine the positions of the absorption lines in the spectrum and therefore the velocity offset with respect to the 3S field, opposite the nucleus. By averaging the two velocities from these field we find $V_{\mathrm{sys}} = 938 \pm 16$ km/s. However, repeating this exercise for the field pair at 3.5 R_e, which are 4S and 4N,

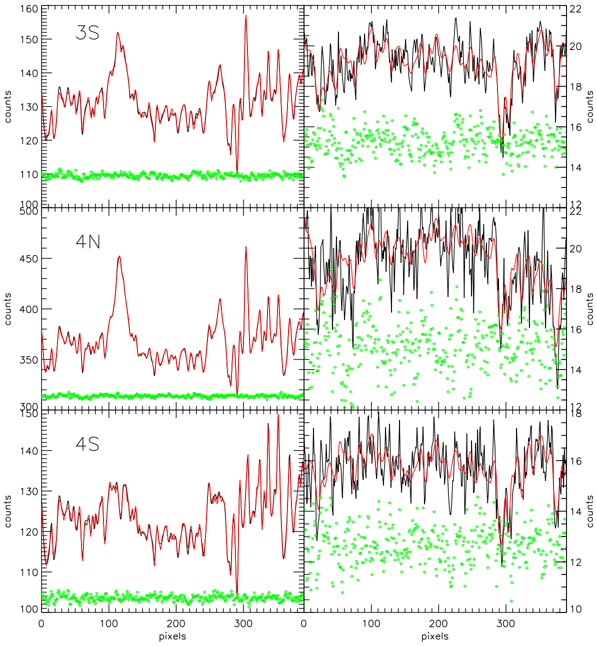

Figure 3.3 — Spectra of our fields in NGC 3379. The left panels show the observed spectra (not skysubtracted) in black, with overplotted in grey the best fit from pPXF (combination of stellar template broadened with LOSVD and scaled sky templates). The residuals (diamonds) are offset for presentation purposes. Right: skysubtracted spectra (black) with the same broadened LOSVD (grey) as in the left panels. Residuals are again shown as diamonds.

we find $V_{\text{sys}} = 892 \pm 23$ km/s, which seems marginally deviant from our other two measurements, although this is just outside the 1-σ interval. We therefore decided to subtract for each field pair their own corresponding systemic velocity.

In Figure 3.4 we compare our results with the long-slit data of Statler & Smecker-Hane (1999). The radial extent of the absorption line kinematics has been increased by a factor two compared to the long-slit data, and our data show a smooth continuation of kinematics out to larger radii. We see little rotation at large radii, and the dispersion profile remains flat out to 3.5 R_e, although there is a hint that the profile is slightly dropping. We also plot the kinematic profiles of the planetary nebulae, as presented in Coccato et al. (2009). We folded these profiles to negative radii, to allow comparison with our data at large radii also in these ranges. We find a good agreement between the several datasets, although the rotational velocities found by the planetary nebulae seem to be a bit higher ($\sim$30 km/s) than our findings.

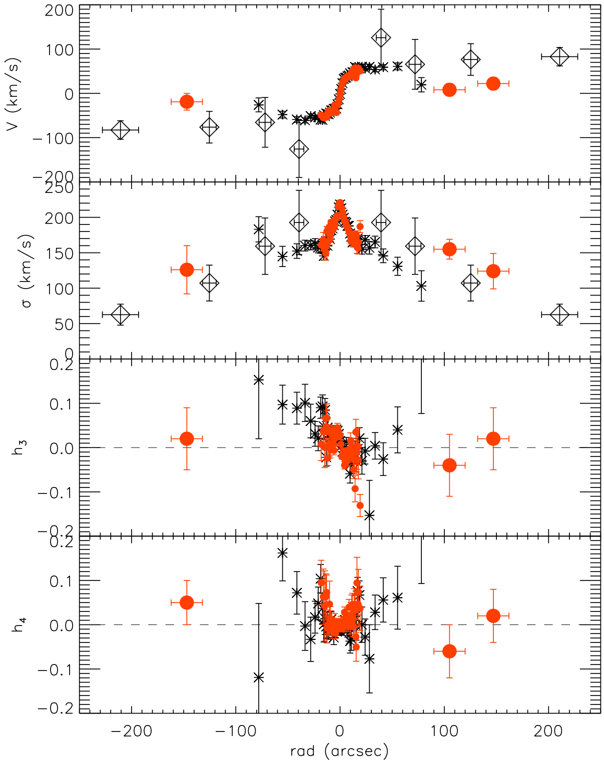

Figure 3.4 — Kinematic profiles along the major axis of NGC 3379. The small grey dots denote the central SAURON data from the original survey and the big red dots are our data at large radii. For comparison, we also plot the long-slit data of Statler & Smecker-Hane (1999) with black stars and the planetary nebulae profiles as presented by Coccato et al. (2009) with open diamonds. The horizontal error bars for the SAURON data at large radii indicate the width of the SAURON field-of-view (30 arcsec), while the horizontal error bars of the PNe data indicate the radial range containing 68 per cent of the PNe used to calculate the kinematics.

3.3.3 NGC 821

The spectra and results for our fields in NGC 821 can be found in Figure 3.5 and Table 3.4. Unfortunately, weather conditions did not allow us to obtain enough signal to measure the LOSVD in all our observed fields, but at each radius one suitable spectrum could be obtained. The systemic velocity from the central kinematics (Emsellem et al. 2004) is 1726 ± 2 km/s (barycentric corrected). This is in agreement with V_{sys} measured from our two field pairs at 1.9 R_e (2S and 2N), where we find a value of 1704 ± 25 km/s. Unfortunately, we could not measure V_{sys} from our field pair at 2.9 R_e due to lack of signal in field 3N. However, our field at the minor axis of NGC 821 gives an independent determination of V_{sys}, assuming axisymmetry so that here the rotational velocity should be zero. We then find $V_{\text{sys}} = 1710 \pm 7$ km/s and $V_{\text{sys}} = 1716 \pm 7$ km/s, depending on whether we fit up the LOSVD up to h_4 or only the first two moments, respectively. Since all these measurements of V_{sys} agree within the errors, we fixed V_{sys} such that the velocity measured on the minor axis is zero.

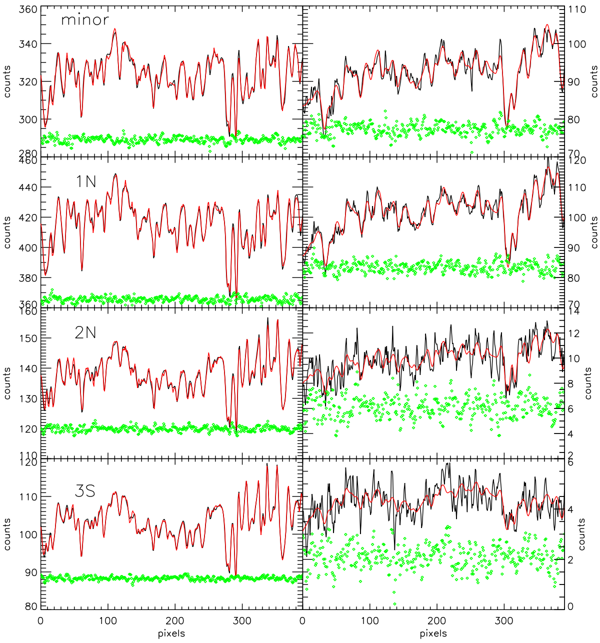

Figure 3.5 — Same as Figure 3.3, but now for our fields in NGC 821.

Figure 3.6 compares our result with the long-slit data of Forestell & Gebhardt (2008). We note that especially in the centre there seem to be some deviations between this dataset and the SAURON data. Differences in sampling between the two datasets (nearly-round bins for the SAURON data versus long, elongated bins for the long slit data) could in principle result in differently-weighted values, but we expect that this effect is small. The most likely cause for the observed deviations are differences in fitted wavelength interval and stellar templates. Also shown are the results from Coccato et al. (2009), who re-analysed the planetary nebulae data that were previously presented by Romanowsky et al. (2003). These data are in good agreement with our stellar kinematics at large radii.

3.4 Line strengths

To measure the absorption line strengths in our spectra, we follow the procedure outlined in Kuntschner et al. (2006). Briefly, we can measure three Lick indices in the SAURON wavelength range: Hβ, Fe5015 and Mg b, defined in Table 2 of Kuntschner et al. (2006). We do not need to remove emission lines from our

Field	Δx (arcsec)	Δy (arcsec)	V (km/s)	δV (km/s)	σ (km/s)	$\delta\sigma$ (km/s)	h_3	δh_3	h_4	δh_4	V_{mean} (km/s)	δV_{mean} (km/s)	σ_{mean} (km/s)	$\delta\sigma_{\mathrm{mean}}$ (km/s)
3S	-77	-77	8	14	155	14	-0.04	0.07	-0.06	0.06	5	11	147	12
4N	104	104	-19	19	126	34	0.02	0.07	0.05	0.05	-16	19	134	35
4S	-104	-104	22	14	124	25	0.02	0.07	0.02	0.06	23	14	127	19

Table 3.3 — Stellar kinematics at large radii for NGC 3379. Δx and Δy denote the offsets (East and North, respectively) from the nucleus of the galaxy to the centre of our observed fields. The quoted errors are 1-σ errors, determined from Monte Carlo simulations. V_{mean} and σ_{mean} are derived by fitting only the first two moments of the LOSVD.

Field	Δx (arcsec)	Δy (arcsec)	V (km/s)	δV (km/s)	σ (km/s)	$\delta\sigma$ (km/s)	h_3	δh_3	h_4	δh_4	V_{mean} (km/s)	δV_{mean} (km/s)	σ_{mean} (km/s)	$\delta\sigma_{\mathrm{mean}}$ (kms/)
minor	33	-21	0	7	171	8	0.07	0.04	0.00	0.04	0	7	168	7
1N	19	30	119	10	174	8	0.00	0.03	-0.04	0.04	112	9	170	7
2N	39	63	72	20	131	22	-0.02	0.07	0.02	0.06	64	18	135	19
3S	-60	-96	-1	28	163	43	-0.02	0.06	0.04	0.06	-8	27	162	38

Table 3.4 — Stellar kinematics at large radii for NGC 821, similar to Table 3.3.

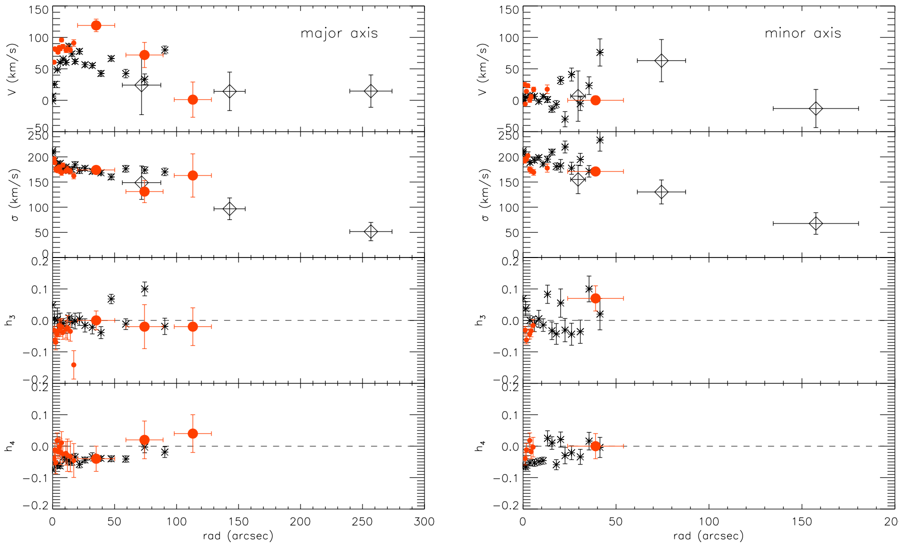

Figure 3.6 — Kinematic profiles along the major (left) and minor (right) axis of NGC 821. As in Figure 3.4, small grey dots are the central SAURON data of the original survey, big grey dots are our data at large radii and open diamonds denote planetary nebulae kinematics from Coccato et al. (2009). The black stars are long-slit stellar kinematics from Forestell & Gebhardt (2008). Horizontal error bars are as described in Figure 3.4.

spectra, since our galaxies show no sign of ionised gas outside the central regions (Sarzi et al. 2006). To calibrate to the Lick/IDS system, we broaden our spectra to an instrumental resolution of σ = 212 km s^{-1}. We correct our measured line strengths for the broadening caused by the LOSVD and we apply the offsets from Table 3 in Kuntschner et al. (2006) to correct for differences in the shape of the continuum, since the Lick/IDS spectra have not been flux calibrated.

We noticed that the continuum shape blue-ward of the Hβ feature in our spectra was affected by bad flatfielding or wrong sky subtraction. We therefore applied the same continuum correction as was done in Kuntschner et al. (2006) and fitted an 11th order multiplicative polynomial together with an optimal stellar template to our spectra. The template had been broadened with the observed LOSVD. We then divided our observed spectrum by this polynomial, before determining the Hβ index.

Field	Hβ (Å)	error (Å)	Fe5015 (Å)	error (Å)	Mg b (Å)	error (Å)
NGC 821						
minor	1.61	0.22	3.80	0.28	3.13	0.16
1N	1.30	0.20	4.11	0.24	3.45	0.17
2N	1.19	0.81	5.16	1.37	5.47	0.64
3S	0.00	1.19	12.0	1.71	6.43	0.76
NGC 3379						
3S	1.49	0.45	2.45	0.58	3.42	0.26
4N	2.13	0.92	2.66	0.86	3.05	0.45
4S	1.17	0.51	2.46	0.66	3.61	0.43

Table 3.5 — Line strengths indices in our observed fields in NGC 821 and NGC 3379.

3.4.1 Results

We present our results for NGC 3379 and NGC 821 in Table 3.5. Errors are estimated with Monte Carlo simulations, where we add noise to our spectra (defined by the difference between our observed and fitted spectra, see Figures 3.3 and 3.5) and vary the bandpasses of the index and the continuum to take the uncertainty in radial velocity into account.

A possible source of contamination for our line strength measurements is the [O III] emission of planetary nebulae. From the catalog of Douglas et al. (2007), each of our fields in NGC 3379 contains one to two planetary nebulae. Following Sarzi et al. (2005), their Equation 1, we should be sensitive to emission lines with EW > 0.7 Å. We carefully checked the individual spectra in each cube, prior to co-adding, and found no evidence for such emission.

We also investigated the effect of sky subtraction on the determinations of line strength. By varying the amount of sky that we subtracted from our spectra, we found that our measurements of Hβ and Fe5015 are quite robust against an error in sky subtraction, even if the skylevels are varied by 10 per cent. Mg b is however already severely affected by a sky subtraction error of only two per cent (see Figure 3.7). This may be due to the proximity of the solar Mg b absorption feature present in the sky spectrum. Our Fe5015 and Mg b indices at 2 and 3 R_e in NGC 821 are unrealistically high, and therefore could be suffering from this problem, although variations in the continuum shape of the spectrum also play a role (see next section). The indices at 1 R_e in this galaxy are less affected, and are in agreement with Proctor et al. (2005). They determined line strengths

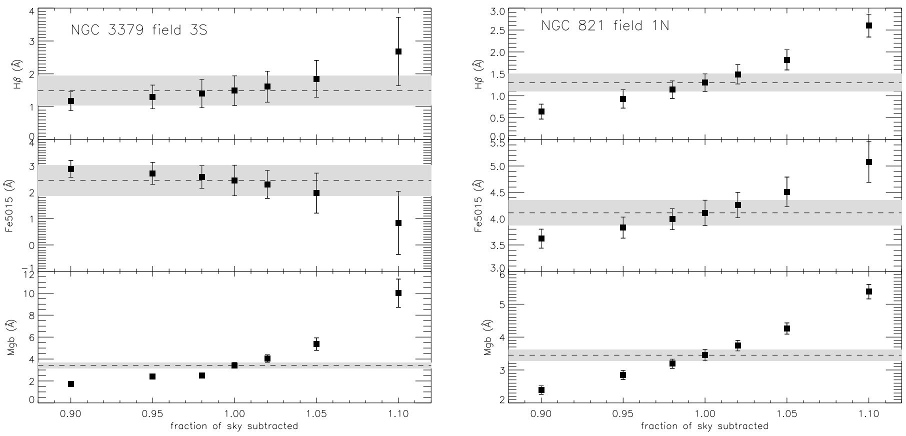

Figure 3.7 — The effect of sky subtraction on our line strength measurements, for the field 3S in NGC 3379 (left) and the 1N field in NGC 821 (right). The x-axis denotes the fraction of sky subtracted. The dashed line indicates the line index when the sky is totally removed, while the grey box denotes the 1-σ interval. Hβ and Fe5015 are robust against an error in sky subtraction up to 5 per cent, though oversubtracting is more severe than undersubtracting. Mg b is very sensitive to sky subtraction errors.

from long-slit data in this galaxy out to 1 R_e. We are not aware of studies in the literature where line strengths have been determined outside 1 R_e for these galaxies, to compare our results with.

3.4.2 Line strength gradients

Line strength gradients are key instruments to study the formation history of galaxies, since different formation models predict different gradients. Monolithic collapse models (Carlberg 1984) produce steep metallicity gradients and a metal-rich nucleus, while hierarchical models show shallower gradients, as mergers dilute existing line strength gradients (White 1980). However, subsequent starformation induced by gas-rich mergers can steepen the gradients again, at least in the central regions (Hopkins et al. 2009a).

Our measurements allow us to study line strength gradients out to large radii. Many previous studies of galaxy samples (e.g. Davies, Sadler & Peletier 1993; Kuntschner et al. 2006; Sánchez-Blázquez et al. 2007) have been limited to ~ 1 R_e, but showed that typically for galaxies without contributions from young stellar populations, Hβ remains flat or increases slightly with radius, while the metal line strengths have negative gradients.

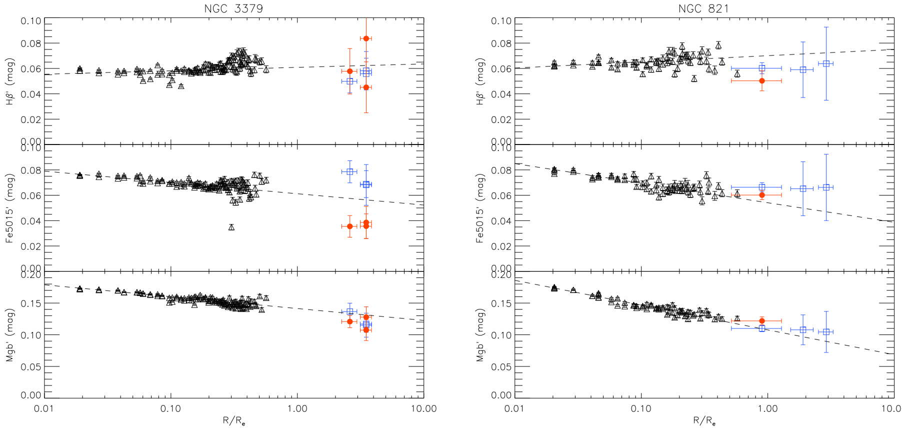

Figure 3.8 — Line strength indices Hβ, Fe5015 and Mg b (in magnitudes) as a function of radius. Left panel: NGC 3379, right panel: NGC 821. Black triangles show indices measured on the SAURON central field, taken from a slit positioned on the major axis of the galaxy, with a width of 2 arcsec. Grey filled dots show our large radii results, and the horizontal error bars denote the size of the SAURON field of view. The points at 2 and 3 R_e in NGC 821 cannot be considered reliable, probably because of continuum shape problems, and therefore are not shown here. The open squares denote our measurements directly from templates of single stellar population models, see text for details. Overplotted is the best fitting linear relation between index and log(radius), determined within $R_e/4$.

To calculate the line strength gradients in our two galaxies, we follow Kuntschner et al. (2006) and first convert our indices from Å to magnitudes:

$$\text{index}' = -2.5\log(1 - \frac{\text{index}}{\Delta\lambda}), \tag{3.2}$$

with $\Delta\lambda$ the width of the index bandpass in Å. Indices expressed in magnitudes will from now on be indicated by a prime sign [$'$]. Line strength gradients are then defined as:

$$\Delta\text{index}' = \frac{\delta\text{index}'}{\delta\log(R/R_e)}. \tag{3.3}$$

We show in Figure 3.8 our line strength indices in magnitudes as a function of radius, with red dots. Also plotted are the values for the central SAURON fields (Kuntschner et al. 2006), which fall within a 2 arcsec wide slit positioned along the major axis of the galaxy. We fitted a linear relation between each index and log(radius) within $R_e/4$, to determine the gradient. These gradients are overplotted in the figure, and are compared to our measurements at large radii.

With our new data, we confirm in NGC 3379 the trends mentioned above, that Hβ mildly increases and Fe5015 and Mg b decrease with radius. This indicates that the metallicity in the galaxy keeps decreasing linearly with log(radius) when going from the centre out to larger radii. The gradients for Hβ and Mg b seem to remain constant out to 4 R_e, but Fe5015 falls off more steeply. This would imply an unrealistically high α-enhancement at large radii. To check whether our Fe5015 measurements are affected by continuum shape problems, we did the following test. We remeasured the kinematics in our spectra with pPXF, but this time used the stellar model library of Vazdekis et al. (2007) based on the MILES library (-1.68 $< Z/H <$ 0.0; 1 Gyr $<$ age $<$ 17.78 Gyr) and multiplicative instead of additive polynomials, to allow for a varying continuum shape. The resulting kinematics were consistent with our previous finding. The line strengths were then measured on the composite best-fitting stellar template, without the multiplicative polynomials. The results are also shown in Figure 3.8, as blue squares. For Hβ and Mg b both the direct measurements and the measurements on the stellar templates give similar results, but the values for Fe5015 are higher and consistent with the observed gradient in the central part of the galaxy. We therefore conclude that indeed our measurements for Fe5015 suffer from changes in continuum shape, but that our values for Hβ and Mg b are robust. For NGC 821 we see a similar effect.

Our observation that the line strength gradients are constant out to large radii provides constraints for the merger and star formation history of the galaxy. After a gas-rich merger, star formation in the central regions of the remnant is expected to steepen the gradients, while at larger radii violent relaxation flattens them, though over time ($\sim$ 3 Gyr) the steep gradients in the central part get weaker (Hopkins et al. 2009a; Hopkins et al. 2009b).

3.4.3 Stellar population models

Using the stellar population models of Thomas, Maraston & Bender (2003) and Schiavon (2007), we explore the single stellar population (SSP) equivalent age and metallicity in NGC 3379 and NGC 821 at large radii. Following the aproach of Thomas et al. (2003) we define an abundance ratio insensitive metallicity index similar to their [MgFe]' index by using the Mg b and Fe5015 indices available

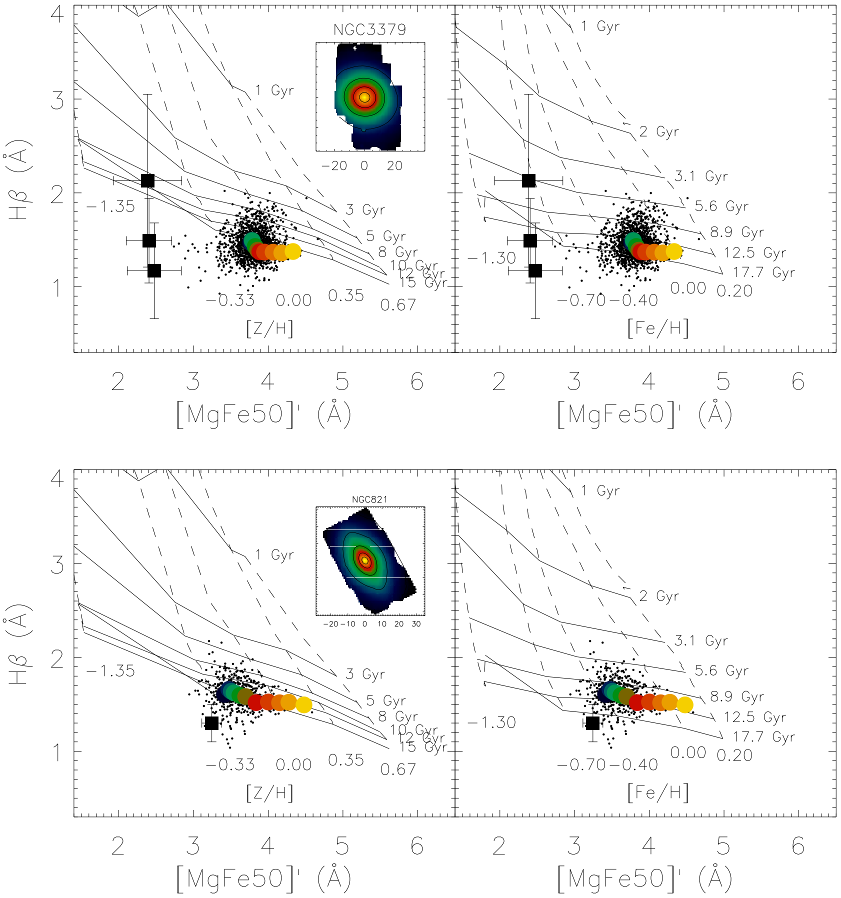

Figure 3.9 — Hβ index against [MgFe50]$'$ (both in Å) in NGC 3379 (top) and NGC 821 (bottom). Left panels show the Thomas et al. (2003) stellar population models (solid and dashed lines) and right panels the Schiavon (2007) models. Black dots indicate measurements from the SAURON central field, while the grey dots are averaged along isophotes (see inset for grey-scale coding). The black filled squares show the data at large radii, revealing an old (12 Gyr) and metal-poor (below 20 per cent solar metallicity) population for both models, though the uncertainties in these values are large. See colour supplement for a colour version of this figure.

from SAURON. [MgFe50]' is defined as:

$$[\mathrm{MgFe50}]' = \frac{0.69 \times \mathrm{Mg}b + \mathrm{Fe5015}}{2}. \tag{3.4}$$

The scaling factor for the Mg *b* index was optimized such that the mean difference between solar and non-solar ratio model predictions from Thomas et al. (2003) is zero. In Figure 3.9 we plot this index versus Hβ and compare with the models. Even though the models of Thomas et al. (2003) and Schiavon (2007) are constructed independently, using different stellar libraries and fitting functions, they give the same results for our data at large radii. For NGC 3379 we find that at 3 - 4 R_e, the stellar population is consistent with an old (12 Gyr) population, and metal-poor, with [Z/H] slightly below 20 per cent of the solar metallicity. We note however that the uncertainty in these values is rather large. For NGC 821, we find that at 1 R_e the stellar population is of the same age and metallicity range as obtained from the outer bins of the SAURON central field ($\sim$ 0.6 R_e).

Stellar population models predict a decrease in stellar mass-to-light ratio M_*/L if the metallicity of the stellar population decreases, since the stars then become bluer and therefore brighter in the optical. For instance, for a change in metallicity from 0.0 to -0.84 at a constant age of 10 Gyr (consistent with our observervations), M_*/L decreases by about 23 per cent in the models of Maraston (2005). However, for increasing stellar age at constant metallicity, M_*/L also increases. Given this degeneracy and uncertainties, we adopt a constant stellar M/L while constructing the dynamical mass models that we present in the next section. Furthermore, M_*/L depends strongly on Hβ (see e.g. Cappellari et al. 2006). Since the Hβ profiles in our galaxies are nearly flat out to large radii, variations in M_*/L are most likely small.

3.5 Dynamical models

To explore whether our data of NGC 3379 and NGC 821 are consistent with a dark matter halo, we model these galaxies with the triaxial Schwarzschild code presented by van den Bosch et al. (2008). Orbits are calculated within an a priori specified triaxial potential, and a superposition of orbits is determined that best fits the observed kinematics, using the observed surface brightness and self-consistency as constraints. This way, the viewing directions, stellar mass-to-light ratio M_*/L, central black hole mass $M_\bullet$ as well as the internal orbital structure can be determined (see also van de Ven, de Zeeuw & van den Bosch 2008; van den Bosch & van de Ven 2009). Within the limits of the observed photometry and LOSVD, the velocity anisotropy of the galaxy can vary freely.

3.5.1 Including a dark halo

We extended the triaxial Schwarzschild code by adding a dark matter halo to the gravitational potential, which already consisted of a stellar contribution inferred from the observed photometry and a Plummer potential for the contribution of the central black hole (see van den Bosch et al. 2008 for more details). We parametrise the dark halo with a spherical NFW profile (Navarro, Frenk & White 1996):

$$\rho(r) = \frac{\rho_s}{r/r_s(1+r/r_s)^2}, \tag{3.5}$$

with ρ_s the characteristic density of the halo and r_s a characteristic radius. The potential generated by this density distribution is then given by:

$$\Phi(r) = -4\pi G\rho_s r_s^2 \frac{r_s}{r} \ln(1+\frac{r}{r_s}), \tag{3.6}$$

where G is the gravitational constant.

We are interested in the presence and acceptable mass range of the halo; modeling the shape of the halo in detail is beyond the scope of this paper. We therefore fix the concentration $c = r_{200}/r_s$ of the halo to 10, as indicated by cosmological simulations (Bullock et al. 2001). Here r_{200} is the radius of the halo within which the mean density has dropped to 200 times the critical density $\rho_{\rm crit}$. It can be shown that

$$\frac{\rho_s}{\rho_{\rm crit}} = \frac{200}{3}\frac{c^3}{\ln(1+c)-c/(1+c)}, \tag{3.7}$$

such that c determines ρ_s in the potential of Equation 3.6. We vary the halo mass,

$$M_{200} = 4\pi\rho_s r_s^3 \left[\ln(1+c) - \frac{c}{1+c}\right], \tag{3.8}$$

which is the enclosed mass within r_{200}, yielding r_s. We only fit for M_{200} and keep M_*/L fixed to the maximum value allowed by the data, therefore fitting a minimal halo or maximal spheroid[2]. The influence of the black hole is negligible at large radii and therefore we also do not fit for $M_\bullet$ but keep its value fixed.

---

[2] Comparable to the maximal disc model that is often invoked when modeling dark haloes of spiral galaxies.

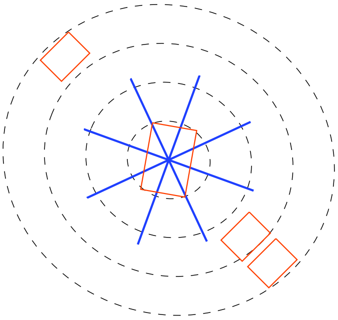

Figure 3.10 — Overview of the datasets included in our dynamical model of NGC 3379. The dotted lines denote isophotes of the galaxy at 1, 2, 3 and 4 R_e. The box in the centre denotes the central SAURON field (Emsellem et al. 2004), while the other boxes show the positions of our data at large radii. The solid lines show the orientation and extent of the long-slit data (Statler & Smecker-Hane 1999).

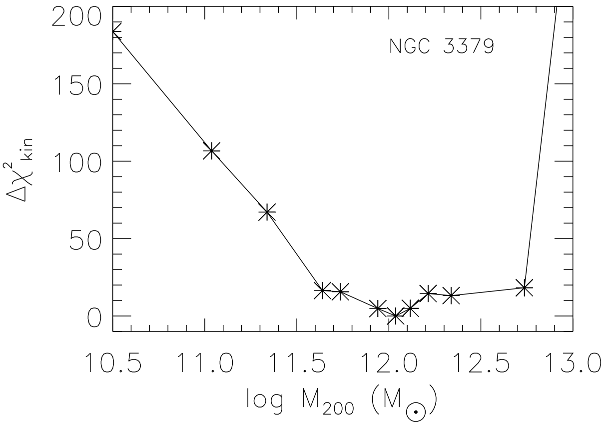

Figure 3.11 — $\Delta\chi^2$ levels for the Schwarzschild models we ran for NGC 3379. The only free parameter in these models was M_{200} (total halo mass). The model without dark halo is relocated at $3 \times 10^{10} M_\odot$, to place it within the plot.

3.5.2 Modelling NGC 3379 and NGC 821

NGC 3379 has a small kinematic misalignment of $5 \pm 3°$ (e.g. Statler & Smecker-Hane 1999) and shows signs of a kinematic twist (Krajnović et al. 2008), which indicate that the galaxy is not perfectly axisymmetric (see also Capaccioli et al. 1991; Statler 2001). Van den Bosch & de Zeeuw (2009) therefore constructed triaxial Schwarzschild models of this galaxy. Their best-fitting triaxial model (axis ratios $p = 0.95$, $q = 0.81$) is nearly face-on, with an inclination of $\sim 40°$. This model is nearly spherical in the centre and becomes close to oblate at large radii, which is in agreement with Statler (2001) and De Lorenzi et al. (2009).

We adopt the best-fit model of van den Bosch & de Zeeuw (2009) for our halo modeling. The model has a black hole mass of $M_\bullet = 4.0 \times 10^8 M_\odot$ and a dynamical mass-to-light ratio $M/L_I = 2.9\ M_\odot/L_{I,\odot}$, which we adopt as the maximally allowed stellar mass-to-light ratio M_*/L. The stellar potential is represented by a Multi-Gaussian Expansion (MGE, Emsellem, Monnet & Bacon 1994; Cappellari 2002) model based upon I-band imaging[3], presented by Cappellari et al. (2006). We use the same central SAURON kinematics (up to h_6) extracted with the MILES library (see Shapiro et al. 2006; Cappellari et al. 2007; van den Bosch & de Zeeuw 2009) to cover the inner R_e of NGC 3379 and add our measure points at large radii. For extra spatial coverage, we also include the symmetrized data of the four long-slit observations of Statler & Smecker-Hane (1999) (see Figure 3.10). The large mosaic of central SAURON data provides many more kinematic constraints in the central region than the four slits. We therefore exclude the inner 20 arcsec of each slit from the fit. The planetary nebulae measurements are not based on integrated stellar light, as our SAURON and long-slit data, and therefore for consistency not included.

We use a similar procedure to construct mass models of NGC 821. This galaxy is a very flattened system (E6) and shows no signs of non-axisymmetry in its central part, even though planetary nebulae kinematics suggest twists at larger radii (Coccato et al. 2009). Our dataset however provides no constraints on the behaviour of the velocity field at these scales. We therefore deproject this galaxy axisymmetrically, assuming an edge-on view and use the triaxial code in the axisymmetric limit. We adopt the edge-on MGE model of NGC 821 based upon ground-based R-band photometry[4] and space-based imaging with HST/WFPC2 in F814W-band, as in McDermid (2002) and Cappellari et al. (2006). We first construct a model without a dark halo, based only on kinematics (up to h_6) of the central SAURON dataset, extracted with the MILES library (Cappellari et al. 2007). Our best fit has a stellar mass-to-light ratio of 2.5 $M_\odot/L_{I,\odot}$ with a black hole mass of $M_\bullet = 2.1 \times 10^8 M_\odot$ from the $M_\bullet$-σ relation. We then add a dark NFW halo to this model, with a fixed concentration of $c = 10$. The SAURON central dataset is used to cover the central part of the galaxy, while our four measurepoints at large radii are included to cover the outerparts. To avoid a possible conflict between the central SAURON data and the long-slit data of Forestell & Gebhardt (2008), we decided to not include the latter in our model, as there seem to be some deviations between the two datasets (see Figure 3.6).

---

[3] Obtained with the 1.3-m McGraw-Gill Telescope of the MDM Observatory, Kitt Peak, US.

[4] Obtained with the 0.9-m telescope at the Cerro Tololo Inter-American Observatory (CTIO), Chile.

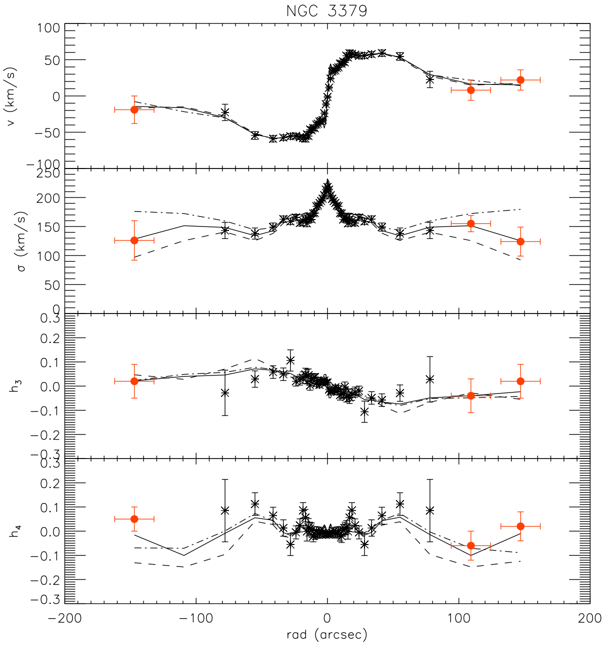

Figure 3.12 — Best-fit model for NGC 3379 (bold line, $M_{200} = 1.0 \times 10^{12} M_\odot$) compared to our datapoints at large radii (grey filled circles) and long-slit data on the major axis (black stars). Also indicated are a model without halo (dashed line) and a model with a heavy halo (dashed-dotted line, $M_{200} = 5.2 \times 10^{12} M_\odot$). These models respectively underpredict and overpredict the observed velocity dispersion.

Our best fitting model for NGC 3379 requires a halo mass of $M_{200} = 1.0 \times 10^{12} M_\odot$, as compared to a total stellar mass of $1.0 \times 10^{11} M_\odot$. In Figure 3.12 we show the kinematics of our best-fit model compared to our data at large radii and the long-slit kinematics on the major axis. The fit is excellent, even for the higher order moments h_3 and h_4. A model without dark halo clearly underpredicts the observed velocity dispersion and h_4 outside 1 R_e. For comparison also a model with a halo heavier than our best fit model is shown: here the velocity dispersion is overestimated. In Figure 3.11 we show the χ^2 values of our best fitting model. We see that with 3-σ confidence, $M_{200} = 1.0^{+0.4}_{-0.3} \times 10^{12} M_\odot$ under the assumptions mentioned above, while a model without dark halo is strongly excluded.

We obtain similar results for NGC 821, where we also exclude the absence of a dark halo (see Figure 3.13). The halo mass in our best-fit model is $M_{200} = 6.5^{+1.0}_{-4.3} \times 10^{11} M_\odot$, while the total stellar mass is $1.1 \times 10^{11} M_\odot$. The kinematics of the fit compared to the observed kinematics are shown in Figure 3.14, where for

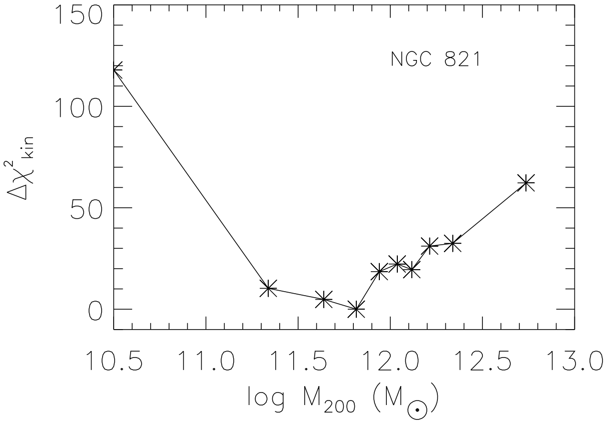

Figure 3.13 — Same as Figure 3.11, but now for NGC 821.

comparison also a model without a dark halo and a model with a too massive halo are shown.

We conclude that dark matter is present both in NGC 3379 and NGC 821. Even within 1 R_e in NGC 3379, 8 per cent of the total mass is dark, while at 4 R_e this fraction has increased to 34 per cent. NGC 821 is more dark matter dominated, with a dark matter fraction of already 18 per cent within 1 R_e, increasing to 49 per cent within 4 R_e. Note however that these values are based on minimal halo assumptions, and therefore should be seen as lower limits. Also, varying halo shape and profile can cause these fractions to change, they therefore should be strictly seen as indicative.

3.5.3 Orbital structure

In the top panels of Figure 3.15 we show the orbital anisotropy in our dynamical models of NGC 3379 and NGC 821. We characterize the orbital anisotropy as

$$\beta_r = 1 - \frac{\sigma_\phi^2 + \sigma_\theta^2}{2\sigma_r^2}, \tag{3.9}$$

with (r, θ, ϕ) standard spherical coordinates. Our best-fit model of NGC 3379 is nearly isotropic within 2 R_e, and at larger radii the radial anisotropy increases. Our best-fit model of NGC 821 is already mildly radially anisotropic in the central regions, but also shows a small increase with radius. Cappellari et al. (2007) presented orbital anisotropy values for both NGC 3379 and NGC 821 from axisymmetric models, based on the same central SAURON data and MGE models

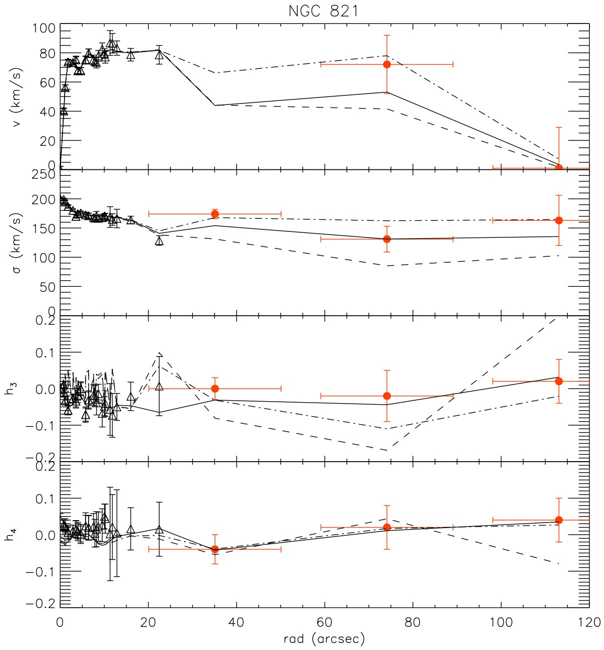

Figure 3.14 — Best-fit model for NGC 821 (bold line, $M_{200} = 6.5 \times 10^{11} M_\odot$) compared to our datapoints at large radii (grey filled circles) and the central SAURON data (open triangles). The dashed line indicates a model without halo and the dashed-dotted line a model with a too heavy halo ($M_{200} = 5.5 \times 10^{12} M_\odot$).

as we use in this paper. Our central anisotropy values are consistent with theirs for both galaxies. Since Cappellari et al. (2007) used a different, independent modeling code, this agreement gives confidence in the robustness of the anisotropy parameters presented here.

Within 1 R_e, the orbital anisotropy changes only marginally between our models with and without halo, consistent with the findings of Thomas et al. (2009). At larger radii the radial anisotropy increases, and the increase is smaller for models with heavier haloes. This is contrary to what is seen in spherical models. In order to fit the observed mildly declining or constant velocity dispersion profile without invoking extra dark matter at large radii, the orbits have to be tangentially anisotropic, while adding a dark halo results in more radially anisotropic orbits (e.g. Richstone & Tremaine 1984; Dekel et al. 2005; de Lorenzi et al. 2009).

The detailed kinematics in the inner part of the galaxy together with our observed positive h_4 in the outer parts already tightly constrain the fraction of box and tube orbits in our triaxial potential, and therefore the anisotropy. Box orbits

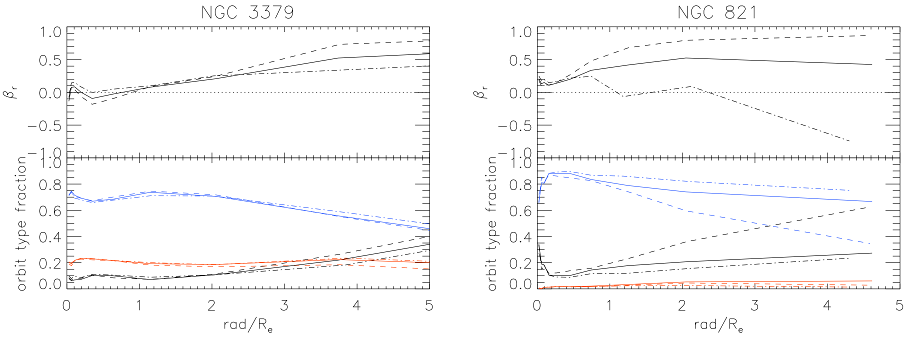

Figure 3.15 — Orbital structure in NGC 3379 (left) and NGC 821 (right). Top panel: velocity anisotropy β_r as a function of radius (see Equation 3.9). The lines are as in Figures 3.12 and 3.14, with the solid line for our best-fit model, the dashed line for the model without halo and the dashed-dotted line for the model with the too heavy halo. Bottom panel: fraction of orbit types as a function of radius for the models of the top panel. Blue lines denote the fractions of short axis tubes, red the fractions of long axis tubes and black the fractions of box orbits. See the colour supplement for a colour version of this figure.

have no net rotation, and contribute to the radial anisotropy of the system, requiring $h_4 > 0$. For tube orbits to reproduce the observed nearly zero mean rotation at large radii, they have to be counter-rotating, increasing the velocity dispersion. However, they would at the same time increase the tangential anisotropy and therefore yield $h_4 < 0$. Since we observe a positive h_4 at large radii, box orbits are expected to contribute significantly to the orbital structure in our models without dark matter, as confirmed in Figure 3.15. As a result, the models without dark halo are strongly radial anisotropic at large radii. Adding a spherical dark matter halo to the system makes the gravitational potential less triaxial. This will decrease the phase space volume of box orbits and naturally results in a larger population of tube orbits (Hunter & de Zeeuw 1992). The radial anisotropy of the system will decrease, as is illustrated in Figure 3.15. This decrease is more pronounced in NGC 821 than in NGC 3379, since our best-fit model of NGC 821 is more dark matter dominated than our NGC 3379 model.

3.5.4 Mg b - $V_{\rm esc}$ relation

We here investigate the connection between the stellar populations and the mass distribution of the galaxy. Franx & Illingworth (1990) showed that there is a tight relation between the local colour (tracing metallicity) and the local escape velocity $V_{\rm esc}$ (tracing the gravitational potential Φ) in early-type galaxies, with $V_{\rm esc}$ given by:

$$V_{\rm esc} = \sqrt{2|\Phi|}. \tag{3.10}$$

This relation was confirmed by Davies et al. (1993), who used Mg 2 as a tracer for metallicity. Scott et al. (2009) find correlations between line strength indices and $V_{\rm esc}$ for the early-type galaxies in the SAURON sample, based on measurements within $\sim$1 R_e. They also show that for Mg *b* this relation does not only hold locally in one galaxy, but is also a global relation between different galaxies.

With our data at large radii we can now investigate the behaviour of this relation out to 4 R_e. We determine for our best-fit model of NGC 3379 the contribution to the gravitational potential of the dark halo using Equation 3.6. The contribution of the stellar mass is inferred from the MGE model, following the formularium in the appendix of Cappellari et al. (2002) and the black hole is included as a Plummer potential. We plot our result in Figure 3.16, and find that the observed relation within 1 R_e continues out to at least 4 R_e. The influence of the dark halo on the Mg *b* - $V_{\rm esc}$ relation becomes clear when comparing our results to a model without a dark halo, where the only contribution to the potential comes from the MGE model and the black hole (open symbols in Figure 3.16). Not only is there an offset in $V_{\rm esc}$ with respect to the model with the dark halo, but also the slope changes, an effect which was also noted by Franx & Illingworth (1990). The addition of extra mass at larger radii by the dark halo deepens the potential well, which means that even particles in the centre of the galaxy will need a larger $V_{\rm esc}$ to climb out of this well, causing a shift in $V_{\rm esc}$ at all radii. However, particles in the outskirts of the galaxy are relatively more affected by the addition of the dark halo than particles in the more central regions: if the halo had not been present, escaping from the potential well at large radii would have been relatively easy. Therefore, the shift in $V_{\rm esc}$ is larger at larger radii, something that is also illustrated by Figure 3.16. The net result is a change in slope. We find that the slope of the Mg *b* - $V_{\rm esc}$ relation in NGC 3379 changes in logscale from 0.31 to 0.46, when taking the dark halo into account. If instead of considering the infinite halo mass of the NFW profile we only take the contribution of the halo within r_{200} into account when calculating the gravitational potential, the slope becomes 0.43 in logscale.

We note that in both the models with and without halo, there is a *local* relation between Mg *b* and $V_{\rm esc}$. However, when looking at a larger sample of galaxies and studying the *global* Mg *b* - $V_{\rm esc}$ relation the contribution of the halo to the potential should be taken into account to interpret the slopes, since the relative contribution

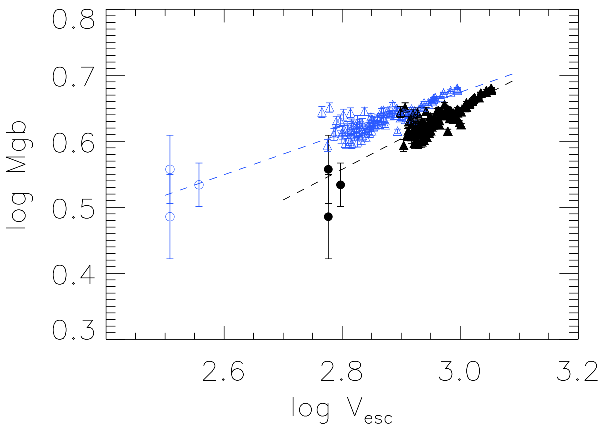

Figure 3.16 — Mg *b* (in Å) versus local escape velocity $V_{\rm esc}$ (km/s) in NGC 3379. Black filled triangles denote points from the central SAURON data, while the black filled dots are our large radii data. Overplotted is the gradient fitted to the central dataset. With open symbols (in grey) we show the Mg *b* - $V_{\rm esc}$ relation calculated from our model without a halo. This relation is offset from our best-fit model and also has a different slope, illustrating the influence of the dark matter.

of the dark matter to the potential compared to the luminous one may vary from galaxy to galaxy, e.g. depending on galaxy mass or environment.

3.6 Summary and conclusion

We used the SAURON IFU as a "photon collector" to obtain stellar absorption line kinematics and line strengths out to four effective radii in the early-type galaxies NGC 3379 and NGC 821. By co-adding the individual spectra of each lenslet into one spectrum for each observed field, we were able to obtain sufficient signal-to-noise in the outskirts of these galaxies, which are too faint to observe with traditional long-slit spectroscopy. The stellar velocity profiles are measured up to the fourth Gauss-Hermite moment (h_4), which allows us to break the mass-anisotropy degeneracy when constructing dynamical models of our galaxies. The kinematics show a smooth continuation of the profiles measured within 1-2 R_e with SAURON and long-slit spectroscopy, and are consistent with planetary nebulae kinematics. The line strengths also show a continuation of the gradients observed within 1 R_e, although our Fe5015 measurements probably suffer from variations in the continuum shape. The stellar halo population is old and metal-poor. The continuation of the line strength gradients and the Mg *b* - $V_{\rm esc}$ relation out to at least 4 R_e provides constraints for the star formation and merger history of early-type galaxies (e.g.

Hopkins et al. 2009a; Hopkins et al. 2009b; Spolaor et al. 2009).

Constructing dynamical orbit-based models, we show that even assuming a maximal stellar contribution, both NGC 3379 and NGC 821 require a dark halo to fit the observed kinematics. We parametrised the halo contribution with a spherical NFW profile, fixing the concentration to $c = 10$. We therefore cannot give a definite number for the precise mass content, shape and anisotropy of the halo. Varying c in our halo profile does not have a large effect on the fitted dark matter content, as an increase of c will be accompanied by a decrease in M_{200}, as the dynamical models constrain the density inside the region for which kinematics are available. Only with data at even larger radii (preferably out to $\sim 100\ R_e$, accessible with e.g. weak gravitational lensing or satellites) we would be able to break the degeneracy between c and M_{200}. In that sense, our results should be viewed as an estimate of the minimal contribution of the dark halo to the total mass budget in the galaxy, and we then see that even at small radii (within $1\ R_e$), the dark matter is already responsible for 10 - 20 per cent of the total mass. These percentages will increase if we relax the minimal halo assumption, but we then need reliable measurements of the stellar mass-to-light ratio and its potential variation with radius. With better spatial coverage of the galaxy, either by mosaicing or by employing larger IFUs (such as VIRUS-P and in the future MUSE) and combining the so-obtained stellar kinematics with other datasets tracing dark matter at different regimes (e.g. H I discs or rings, hot gas, gravitational lensing and/or discrete tracers such as planetary nebulae) we will be able to build more sophisticated dynamical models, to explore the shape and mass of the dark haloes around early-type galaxies.

Acknowledgements

It is a pleasure to thank Eveline van Scherpenzeel, Chris Benn and the ING staff for support on La Palma. We gratefully acknowledge Koen Kuijken, Aaron Romanowsky and Marc Sarzi for fruitful discussions. We also thank Richard Wilman for supplying us with the data necessary to make the superflat for NGC 3379 and Lodovico Coccato for sending us the planetary nebulae kinematic profiles of NGC 821 and NGC 3379. We are grateful to the referee, Elena Terlevich, for constructive comments which improved the presentation of the paper.

This research was supported by the Netherlands Organization of Scientific Research (NWO) through grants 614.000.426 and 614.000.301. AW acknowledges The Leids Kerkhoven-Bosscha Fonds for contributing to working visits, as well as the hospitality of ESO, the University of Oxford, l'Observatoire de Lyon and the Institute for Advanced Study. MC acknowledges support from a PPARC Advanced Fellowship (PP/D005574/1). GvdV acknowledges support through Hubble Fellowship grant HST-HF-01202.01-A awarded by the Space Telescope Science Institute, which is operated by the Association of Universities for Research in Astronomy, Inc., for NASA, under contract NAS 5-26555.

The SAURON observations were obtained at the William Herschel Telescope, operated by the Isaac Newton Group in the Spanish Observatorio del Roque de los Muchachos of the Instituto de Astrofísica de Canarias.